

Quantum transport of two-species Dirac fermions in dual-gated three-dimensional topological insulators

Authors: Yang Xu^{1,2}, Ireneusz Miotkowski¹, Yong P. Chen^{1,2,3,*}

Affiliations:

¹Department of Physics and Astronomy, Purdue University, West Lafayette, IN 47907 USA.

²Birck Nanotechnology Center, Purdue University, West Lafayette, IN 47907 USA.

³School of Electrical and Computer Engineering, Purdue University, West Lafayette, IN 47907 USA.

*Correspondence to: yongchen@purdue.edu

Abstract: Topological insulators are a novel class of quantum matter with a gapped insulating bulk yet gapless spin helical Dirac fermion conducting surface states. Here, we report local and non-local electrical and magneto transport measurements in dual-gated BiSbTeSe₂ thin film topological insulator devices, with conduction dominated by the spatially separated top and bottom surfaces, each hosting a single species of Dirac fermions with independent gate control over the carrier type and density. We observe many intriguing quantum transport phenomena in such a fully-tunable two-species topological Dirac gas, including a zero-magnetic-field minimum conductivity close to twice the conductance quantum at the double Dirac point, a series of ambipolar two-component half-integer Dirac quantum Hall states and an electron-hole total filling factor zero state (with a zero-Hall plateau), exhibiting dissipationless (chiral) and dissipative

(non-chiral) edge conduction respectively. Such a system paves the way to explore rich physics ranging from topological magnetoelectric effects to exciton condensation.

Introduction

A three-dimensional topological insulator (TI) is characterized by an insulating bulk band gap and gapless conducting topological surface states (TSS) of spin-helical massless 2D Dirac fermions^{1,2}. Such surface states are topologically non-trivial and protected by time-reversal symmetry, thus immune to back scattering. The potential novel physics offered by this system, such as topological magnetoelectric (TME) effects^{3,4}, Majorana fermions⁵, and effective magnetic monopoles⁶, has drawn intense interest. One of the most iconic transport signatures for 2D Dirac electronic systems is the half-integer quantum Hall effect (QHE) in a perpendicular magnetic field (B), as first observed in graphene^{7,8} and later also studied in HgTe^{9,10}. The Landau Levels (LL) of 2D Dirac fermions have energies $E_N = \text{sgn}(N)v_F(2eB\hbar|N|)^{1/2}$, where sgn is the sign function, N is the LL index (positive for electrons and negative for holes), v_F is the Fermi velocity, e is the elemental charge and \hbar is the Plank's constant h divided by 2π . The zeroth LL at $E_0=0$ is equally shared between electrons and holes, giving rise to the half-integer shift in the quantized Hall conductivity $\sigma_{xy} = g(N+1/2)e^2/h$, where g is the number of degenerate species of Dirac fermions (e.g., $g=4$ for graphene, and $g=1$ for TSS with a single Dirac cone). This $1/2$ can also be related to the Berry-phase due to the spin or pseudospin locking to the momentum of Dirac fermions⁷⁻¹⁰.

In most commonly studied TI materials such as Bi_2Se_3 , Bi_2Te_3 and other Bi/Sb-based chalcogenides, it is often challenging to observe characteristic TSS transport (particularly QHE) due to bulk conduction caused by unintentional impurity doping. Only very recently has well-developed QHE arising from TSS been observed in exfoliated flakes from BiSbTeSe_2 (BSTS) single crystals¹¹ and molecular beam epitaxy grown $(\text{Bi}_{1-x}\text{Sb}_x)_2\text{Te}_3$ or Bi_2Se_3 thin films^{12,13}. In this work, we fabricate dual-gated^{14–16} TI devices from exfoliated BSTS thin flakes with undetectable bulk carrier density and conduction at low temperature¹¹. Such a dual-gating structure is also promising for exploring exciton condensation proposed for TIs¹⁷ and topological quantum phase transitions induced by displacement electric field¹⁸.

In our dual-gated BSTS devices, the independent, ambipolar gating of parallel-conducting top and bottom surfaces realize two independently-controlled species of 2D Dirac fermions, allowing us to investigate such interesting transport phenomena as the minimum conductivity of TSS at Dirac point (DP), and two-species (two-component) Dirac fermion QHE of electron+electron, electron+hole and hole+hole types, involving various combinations of top and bottom surface half-integer filling factors ν_t and ν_b . When $(\nu_t, \nu_b) = (-1/2, 1/2)$ or $(1/2, -1/2)$, there's an intriguing $\nu=0$ state characterized by zero Hall plateau and a large longitudinal resistance peak^{11,12}, attributed to the formation of dissipative and non-chiral edge states. We also perform non-local transport measurements and compare that with the normal local measurements in our dual-gated 3D TI devices in the quantum Hall regime to probe the nature of edge state transport for both standard QH states and the novel $\nu=0$ dissipative QH-like state. We further

demonstrate that the dissipative edge states at $\nu=0$ have temperature-independent conductance, revealing that the transport in such a quasi-1D dissipative metallic edge channel could evade standard localization.

Results

Transport properties at zero and low magnetic field. Qualitatively similar data are measured in multiple samples, while results from a typical sample A (channel length $L=9.4\ \mu\text{m}$, width $W=4.0\ \mu\text{m}$, with $\sim 100\ \text{nm}$ -thick BSTS and $40\ \text{nm}$ -thick h-BN as top-gate dielectric, see schematic in Fig. 1a) are presented below unless otherwise noted. The h-BN as a substrate or gate dielectric is known to preserve good electronic properties for graphene, resulting from the atomic flatness and relatively low density of impurities in h-BN¹⁹. The carrier densities of the top and bottom surface of the BSTS flake are tuned by top-gate voltage V_{tg} and back-gate voltage V_{bg} respectively.

Fig. 1b and 1c show the double-gated electric field effect measured at $T=0.3\ \text{K}$. The longitudinal resistivity ρ_{xx} ($=R_{xx} * W/L$, with R_{xx} being longitudinal resistance) at magnetic field $B=0\ \text{T}$ (Fig. 1b) and Hall resistivity ρ_{xy} ($=R_{xy}$, Hall resistance) at $B=1\ \text{T}$ (Fig. 1c) are plotted in color scale as functions of both top and bottom gate voltages (V_{tg} and V_{bg}). The extracted field effect and Hall mobilities are typically several thousands of $\text{cm}^2\text{V}^{-1}\text{s}^{-1}$. A minimum carrier density $n^* \sim 9 \times 10^{10}\ \text{cm}^{-2}$ per surface can be extracted from the maximum Hall coefficient (absolute value) $\sim 3.5\ \text{k}\Omega/\text{T}$ (when both surfaces are slightly n-type or p-type) measured in Fig. 1c. A set of exemplary V_{tg} -sweeps with $V_{\text{bg}}=3\ \text{V}$ is shown in Fig. 1c inset. By adjusting V_{tg} (or V_{bg}), the device can be gated through a R_{xx} peak, identified

as the charge-neutrality DP of the top (or bottom) surface, marked by the blue (or red) dashed lines in Fig. 1b. Gating through the DP, the carriers in the corresponding surface change from hole-like to electron-like (i.e., ambipolar), as evidenced by Hall measurements (Fig. 1c). The slight deviation of the two lines from being perfectly vertical and horizontal arises from the weak capacitive coupling between the top (bottom) surface and the back (top) gate¹⁶. The crossing of these two lines corresponds to the double DP (both surfaces tuned to DP) where ρ_{xx} ($\sigma_{xx}=1/\rho_{xx}$) reaches a global maximum (minimum). Within the gate voltage range used, the carriers predominantly come from the TSS and we observe relatively good particle-hole symmetry in the transport properties (e.g., the symmetrical appearance of ρ_{xx} on both sides of DP in each surface in Fig. 1b and the similar absolute values of the positive and negative maximum Hall coefficient in Fig. 1c).

We have studied 6 dual-gated BSTS devices with different thicknesses (t) and aspect ratios (L/W). These devices are measured at low temperatures ($T < 2$ K) and the results are repeatable after multiple thermal cycles. When both surfaces are tuned to DP, the minimum 2D conductivity σ_{\min} at $B=0$ T exhibits relatively constant value $(3.8 \pm 0.1)e^2/h$ for all the devices measured (with the uncertainty representing 90% confidence interval), whose thicknesses range from ~ 50 to ~ 200 nm and L/W range from 1.3 to 3.5 (Fig. 1d). Our observation indicates that the conductivity at the DP for each major surface (top or bottom) is $\sim 2e^2/h$ (one unit of conductance quantum), within the range of values ($2 \sim 5 e^2/h$) reported by Kim *et al.*¹⁴ on thin flakes of Bi_2Se_3 (~ 10 nm). The better consistency over multiple samples in our dual-gated BSTS devices may be attributed to the more

insulating bulk (whose conduction is immeasurably small at low temperature) and uniformity of the exfoliated BSTS flakes, which are sandwiched between SiO₂ and h-BN to achieve better device stability. The minimum conductivity at DP has also been discussed in graphene with considerable interest^{20–25}.

The experiments in graphene revealed that the minimum conductivity is strongly affected by carrier-density inhomogeneities (puddles) induced by disorder on or near graphene^{24,25}, such as the adsorbates or charged impurities in the substrates. In 3D TIs, one source of impurities likely relevant to the observed quasi-universal minimum conductivity in our dual-gated BSTS devices could be bulk defects (located near surface)^{26,27}, such as those revealed in scanning tunneling microscopy studies²⁸.

Two-component quantum Hall effect. For the rest of the paper, we focus on the transport phenomena in the quantum Hall (QH) regime under a high magnetic field B perpendicular to the top and bottom surfaces. Fig. 2a and 2c show in color scales the longitudinal conductivity σ_{xx} ($=\rho_{xx}/(\rho_{xx}^2 + \rho_{xy}^2)$) and Hall conductivity σ_{xy} ($=\rho_{xy}/(\rho_{xx}^2 + \rho_{xy}^2)$) for Sample A as functions of V_{tg} and V_{bg} at $B=18$ T and $T=0.3$ K. The color plots in (a) and (c) divide the (V_{tg}, V_{bg}) plane into a series of approximate parallelograms, centered around well-developed or developing QH states with vanishing or minimal σ_{xx} (b) and quantized σ_{xy} in integer units of e^2/h (d). These QH parallelograms are bounded by approximately (but slightly tilted) vertical and horizontal lines, which represent the top and bottom surface LLs respectively. By increasing (decreasing) either V_{tg} or V_{bg} to fill (exhaust) one LL on the top or bottom surface, σ_{xy} increases (decreases) by e^2/h ,

taking consecutive quantized values of $\nu e^2/h$, where integer $\nu = \nu_t + \nu_b = N_t + N_b + 1$. The $N_{t(b)}$ is the corresponding top (bottom) surface LL integer index that can be adjusted by top (back) gate to be of either Dirac electrons or holes. In Fig. 2d, different fixed V_{bg} values (from -17 V to 40 V) set ν_b around consecutive half integers -3/2, -1/2, 1/2, 3/2 and 5/2 (such that the bottom surface contributes $\sigma_{xy}^b = \nu_b e^2/h$ to the total σ_{xy}), explaining the vertical shift of e^2/h at QH plateaux of consecutive V_{tg} -sweeps.

It is also notable that in Fig. 2, there are a few states with zero quantized Hall conductivity ($\sigma_{xy}=0$, manifesting as white regions in Fig. 2c, separating the electron-dominated regions in red and the hole-dominated regions in blue) and non-zero σ_{xx} minimum, marked by equal and opposite half-integer values of ν_t and ν_b thus total $\nu=0$, for example $(\nu_t, \nu_b)=(-1/2, 1/2)$, $(1/2, -1/2)$ and $(3/2, -3/2)$. These states with total $\nu=0$, exhibiting zero Hall plateaux (see also Fig. 2d), have non-zero σ_{xx} minimum (Fig. 2a and 2b) but very large R_{xx} maximum (see next, Fig. 3).

Nonlocal transport at $\nu=0$ states. To further characterize the observed QH and $\nu=0$ states, we have performed nonlocal transport measurements of R_{nl} ($=V_{nl}/I$, I is the current and V_{nl} is the non-local voltage, see the schematic measurement setup in the inset of Fig. 3b) as functions of V_{tg} and V_{bg} at $B=18$ T and $T=0.3$ K and compared the results with the standard (local) measurements of the longitudinal resistance R_{xx} (Fig. 3a). It's intriguing that unlike other QH states typified by a zero or minimum in R_{xx} , the states with $\nu=\nu_t+\nu_b=0$ (labeled by (ν_t, ν_b) in Fig. 3a with $\nu_t=-\nu_b=\pm 1/2$ or $\pm 3/2$) are accompanied by a R_{xx} maximum. The best-developed $\nu=0$ states are those at $(\nu_t, \nu_b)=(-1/2, 1/2)$ or $(1/2, -1/2)$,

where R_{xx} reaches ~ 220 k Ω ($\rho_{xx} \sim 100$ k Ω), exceeding the resistance quantum ($h/e^2 \sim 25.8$ k Ω) by an order of magnitude. The nonlocal R_{nl} also becomes very large (~ 100 k Ω) and the similar order of magnitude as R_{xx} at these two $\nu=0$ states while negligibly small at other (ν_t, ν_b) QH states (see Fig. 3b and also the representative cuts in Fig. 3c).

The simultaneously large local and non-local resistance at $\nu=0$ states in the QH regime has been reported in other 2D electron-hole systems^{29,30} and understood in a picture of dissipative edge channels. We emphasize that the pronounced R_{nl} signal cannot be explained from R_{xx} by a classical Ohmic non-local resistance from the stray current connecting the remote leads. Such a contribution ($\sim \rho_{xx} e^{-\pi L/W}$) would decay exponentially with L/W ($=2.4$ in our case), and be three orders magnitude smaller than the local R_{xx} (which is the case at $B=0$ T, Supplementary Fig. 1). As another comparison, the middle panel of Fig. 3c shows the cuts in Fig. 3(a,b) at $V_{bg}=3$ V, crossing the double-DP (also zeroth LL) of both top and bottom surfaces at $(\nu_t, \nu_b)=(0, 0)$, where we observe a relatively large peak in R_{xx} but significantly smaller R_{nl} . Such a result is consistent with the *extended* state transport (at the center of zeroth LL) as the current flows through the bulk of the 2D surface.

From the color plots in Figs. 2 and 3, the parallelogram centered around $(\nu_t, \nu_b)=(-1/2, 1/2)$ state is enclosed by boundaries representing $N_t=0$ and -1 , $N_b=0$ and 1 LLs. Similarly, $(\nu_t, \nu_b)=(1/2, -1/2)$ state is bounded by $N_t=0$ and 1 , $N_b=0$ and -1 LLs. We conclude that such a $\nu=0$ state can exist when the potential difference V between top and bottom surfaces (equivalently the energy separation between top and bottom surface DPs) is in the range

of $0 < |V| < 2E_{0-1}$ ($\approx 2 \times 50$ meV at $B=18$ T, where E_{0-1} is the 0-1 LL separation of TSS Dirac fermions¹¹). The large energy scale of E_{0-1} can help make the $\nu=0$ and $\nu=\pm 1$ QH states observable at significantly elevated temperatures as demonstrated below.

Temperature dependence of the $\nu=0$ and ± 1 states. We have studied the temperature (T) dependence of the QHE and $\nu=0$ states from 0.3 K to 50 K at $B=18$ T (Fig. 4). At each temperature, the bottom surface density is tuned by V_{bg} to set ν_b near 1/2 (dashed lines) or -1/2 (solid lines), and the peaks in local R_{xx} and nonlocal R_{nl} corresponds to $(\nu_t, \nu_b)=(-1/2, 1/2)$ or $(1/2, -1/2)$, respectively (Fig. 4a and 4b, detailed raw data shown in Supplementary Fig. 2). The R_{xx} peaks ($> \sim 150$ k Ω) are seen to be more robust up to the highest temperature ($T=50$ K) measured while R_{nl} peaks decrease rapidly (approximately linearly in T , shown in Fig. 4c) with increasing T and is nearly suppressed above 50 K. We also show the T -dependence of σ_{xx} and σ_{xy} at $(\nu_t, \nu_b)=(-1/2, 1/2)$, $(1/2, -1/2)$, $(1/2, 1/2)$ and $(-1/2, -1/2)$ in Fig. 4e and 4f. The σ_{xy} maintains good quantization at $\nu e^2/h$ ($\nu=0, \pm 1$) up to $T=50$ K while σ_{xx} increases with T (the gate-dependent σ_{xx} and σ_{xy} traces at different temperatures are shown in Supplementary Fig. 3). The σ_{xx} for $\nu=\pm 1$ states is found to show thermally activated behavior at high temperatures¹¹, where the finite σ_{xx} is attributed to the thermal excited 2D surface or 3D bulk carriers. Such carriers can shunt the edge-state transport and suppress the nonlocal R_{nl} response at high T ²⁹. We also note that the σ_{xx} *versus* T curves for $\nu=0$ and $\nu=\pm 1$ states follow the similar trend and have approximately constant separation. We find the averaged separation $\Delta\sigma_{xx}=1/2*[\sigma_{xx}(-1/2,1/2)+\sigma_{xx}(1/2,-1/2)-\sigma_{xx}(1/2,1/2)-\sigma_{xx}(-1/2,-1/2)]$ to be largely T -independent with a

value of $(0.27 \pm 0.01)e^2/h$, which we attribute to the conductivity of the quasi-1D dissipative edge channel.

Discussions

In our measurement setup, the contacts connect to the top, bottom and side surfaces, all of which are probed simultaneously. The side surface only experiences an in-plane field and can be viewed as a quasi-1D domain boundary that separates the top and bottom surfaces with B pointing outward and inward respectively, thus can support QH edge states³¹.

When the top and bottom surfaces are doped to the same carrier type (either n or p), the corresponding QH edge states (on the side surface) would have the same chirality and give the observed total $\sigma_{xy} = \nu e^2/h = (\nu_t + \nu_b) e^2/h$, restricted to integer multiples of e^2/h . When the two surfaces have opposite carrier types but one of them dominates, well-defined QH states with $\nu = \nu_t + \nu_b$ may still be observed, such as the $(-1/2, 3/2)$ state with $\sigma_{xy} = (-1/2 + 3/2)e^2/h = e^2/h$ and vanishing ρ_{xx} . Previous studies in InAs/(AlSb)/GaSb heterostructure based electron-hole systems^{32,33} also revealed QH effect with $R_{xy} = h/(\nu e^2) = h/(\nu_e - \nu_h) e^2$ (ν_e and ν_h are electron and hole filling factors, both are positive integers) and vanishing R_{xx} when the AlSb barrier (separating electron and hole gases) is sufficiently thin to enable electron-hole hybridization. Despite the phenomenological similarities, our QH system is distinctive in the sense that the spatially separated electrons and holes residing on the top and bottom surfaces have *half* integer filling factors, and the hybridization only happens at the side surface.

We show the schematic energy spectrum when the two surfaces are degenerate with $V=0$ ^{34–36} in Fig. 4g, which depicts the Fermi energy E_f inside the 0-1 LL gap and corresponds to the (1/2, 1/2) QH state. For a relatively thick sample such as ours (~ 100 nm \gg magnetic length $l_B=(\hbar/eB)^{1/2} \approx 6$ nm at $B=18$ T), however, it has been suggested that even in the presence of well quantized LLs, a standard TI Hall measurement would exhibit deviations from perfectly quantized values due to conduction through the side surfaces^{31,34–36}. On the other hand, it has also been suggested that when net chiral modes exist (Fig. 4g and 4i show one such net chiral mode), the QH effect may be restored by the local equilibrium between non-chiral edge modes³⁷, possibly explaining the good quantization in σ_{xy} and vanishing ρ_{xx} (also R_{nl}) observed in our experiments.

For the $(\nu_t, \nu_b) = (-1/2, 1/2)$ or $(1/2, -1/2)$ state, the carrier density on the top and bottom surfaces are opposite. Since E_f is within the LL gap on both the surfaces, the finite residual σ_{xx} and large R_{nl} we observed are indicative of dissipative edge transport. We show a schematic energy spectrum³⁸ of this $\nu=0$ state with V slightly smaller than E_{0-1} in Fig. 4h, where the Fermi level E_f resides between the $N_t=-1$ and 0 LL of top surface (marked in blue), thus $\nu_t=-1/2$, and also between the $N_b=0$ and 1 LL of bottom surface, thus $\nu_b=1/2$. Overall, such energy spectrum represents a $(\nu_t, \nu_b)=(-1/2, 1/2)$ and $\nu=0$ state. The E_f crosses an even number (only two shown in this illustrative example in Fig. 4h) of counter-propagating edge modes (arising from sub-bands of the quasi-1D side surface). The disorder can cause scattering and local equilibrium between the counter-propagating modes, giving rise to non-chiral dissipative transport (depicted by a series of conducting loops that can hop between adjacent ones in Fig. 4j) on the side surface with a

large and finite resistance. While the energy spectrum (Fig. 4h) is expected to have a gap (Δ) near the edge (due to the hybridization between top (marked with blue) and bottom (red) surface zeroth LLs and approximately the finite-size confinement-induced gap $\approx \hbar v_F/t \approx 10$ meV opened at DP of the side surface³⁸), we did not observe a truly insulating state with vanishing σ_{xx} and diverging R_{xx} (Figs. 2a, 4a). This is likely due to the disorder potential (spatial fluctuation of DP²⁸) comparable or larger than Δ and thus smearing out this gap (effectively E_f always crosses the non-chiral edge modes). It would be an interesting question for future studies to clarify whether the weak T -dependence (at $T < \sim 50$ K) of the observed conductance (Fig. 4e), similar to the behavior reported in InAs/GaSb based electron-hole systems³⁹, may indicate an absence of localization^{40–43} in such quasi-1D resistive edge channels.

Several recent theories have pointed out that the $\nu=1/2-1/2=0$ state in the TI QH system may bring unique opportunities to realize various novel physics. It has been suggested that both the $\nu=0$ state in TI QHE and an analogous quantum anomalous Hall (QAH) state with zero-Hall-conductance plateau in a magnetic doped TI around the coercive field can be used as platforms to observe the TME effect^{44,45}, where an electric (magnetic) field induces a co-linear magnetic (electric) polarization with a quantized magnetoelectric polarizability of $\pm e^2/2h$. A zero-Hall-plateau state has been recently observed in the QAH case in ultrathin (few-nm-thick) films of $\text{Cr}_x(\text{Bi,Sb})_{2-x}\text{Te}_3$ at low temperature (< 1 K)^{46,47}. In comparison, our samples have much larger thickness ($> \sim 50$ nm, suggested to be preferable for better developed TME effect^{45,48}), and our $\nu=0$ state survives at much higher temperatures (~ 50 K). It has also been proposed that excitonic condensation and

superfluidity can occur in thin 3D TIs at the $\nu=0$ state in QH regime⁴⁹ (in addition to at zero B field¹⁷) induced by spontaneous coherence between strongly-interacting top and bottom surfaces. In future studies, much thinner samples are likely needed to investigate the possibility of such exciton superfluidity.

Methods

Sample preparation. Three-dimensional topological insulator (3D TI) single crystals BiSbTeSe₂ (BSTS) were grown by the vertical Bridgman technique¹¹. BSTS flakes (typical thickness ~ 50 -200 nm) are exfoliated (“Scotch tape method”) onto highly doped Si (p+) substrates (with 300 nm-thick SiO₂ coating), and lithographically fabricated into Hall bar shaped devices with Cr/Au contacts. A thin flake of hexagonal boron nitride (h-BN, typical thickness ~ 10 -40 nm) is transferred¹⁹ on the BSTS flake to serve as a top-gate dielectric and a top-gate metal (Cr/Au) is deposited afterwards. The thickness of BSTS and h-BN flakes are measured by atomic force microscopy.

Transport measurement. Transport measurements are performed with the standard lock-in technique using a low-frequency (< 20 Hz) excitation current of 20 nA in a helium-4 variable temperature system (with base temperature down to 1.6 K) or a helium-3 system equipped with magnetic fields (B) up to 18 T (down to 0.3 K).

References

1. Hasan, M. Z. & Kane, C. L. Colloquium: Topological insulators. *Rev. Mod. Phys.* **82**, 3045–3067 (2010).
2. Qi, X.-L. & Zhang, S.-C. Topological insulators and superconductors. *Rev. Mod. Phys.* **83**, 1057–1110 (2011).

3. Qi, X. L., Hughes, T. L. & Zhang, S. C. Topological field theory of time-reversal invariant insulators. *Phys. Rev. B* **78**, 195424 (2008).
4. Essin, A. M., Moore, J. E. & Vanderbilt, D. Magnetoelectric polarizability and axion electrodynamics in crystalline insulators. *Phys. Rev. Lett.* **102**, 146805 (2009).
5. Fu, L. & Kane, C. L. Superconducting Proximity Effect and Majorana Fermions at the Surface of a Topological Insulator. *Phys. Rev. Lett.* **100**, 096407 (2008).
6. Qi, X.-L., Li, R., Zang, J. & Zhang, S.-C. Inducing a magnetic monopole with topological surface States. *Science* **323**, 1184–1187 (2009).
7. Novoselov, K. S. *et al.* Two-dimensional gas of massless Dirac fermions in graphene. *Nature* **438**, 197–200 (2005).
8. Zhang, Y., Tan, Y.-W., Stormer, H. L. & Kim, P. Experimental observation of the quantum Hall effect and Berry’s phase in graphene. *Nature* **438**, 201–204 (2005).
9. Büttner, B. *et al.* Single valley Dirac fermions in zero-gap HgTe quantum wells. *Nat. Phys.* **7**, 418–422 (2011).
10. Brüne, C. *et al.* Quantum Hall Effect from the Topological Surface States of Strained Bulk HgTe. *Phys. Rev. Lett.* **106**, 126803 (2011).
11. Xu, Y. *et al.* Observation of topological surface state quantum Hall effect in an intrinsic three-dimensional topological insulator. *Nat. Phys.* **10**, 956–963 (2014).
12. Yoshimi, A. R. *et al.* Quantum Hall Effect on Top and Bottom Surface States of Topological Insulator Films. *Nat. Commun.* **6**, 6627 (2014).
13. Koirala, N. *et al.* Record Surface State Mobility and Quantum Hall Effect in Topological Insulator Thin Films via Interface Engineering. *Nano Lett.* **15**, 8245–8249 (2015).
14. Kim, D. *et al.* Surface conduction of topological Dirac electrons in bulk insulating Bi₂Se₃. *Nat. Phys.* **8**, 460–464 (2012).
15. Chang, C.-Z. *et al.* Simultaneous Electrical-Field-Effect Modulation of Both Top and Bottom Dirac Surface States of Epitaxial Thin Films of Three-Dimensional Topological Insulators. *Nano Lett.* **15**, 1090–1094 (2015).
16. Fatemi, V. *et al.* Electrostatic Coupling between Two Surfaces of a Topological Insulator Nanodevice. *Phys. Rev. Lett.* **113**, 206801 (2014).
17. Seradjeh, B., Moore, J. E. & Franz, M. Exciton Condensation and Charge Fractionalization in a Topological Insulator Film. *Phys. Rev. Lett.* **103**, 066402 (2009).
18. Kim, M., Kim, C. H., Kim, H.-S. & Ihm, J. Topological quantum phase transitions driven by external electric fields in Sb₂Te₃ thin films. *Proc. Natl. Acad. Sci.* **109**, 671–674 (2012).
19. Dean, C. R. *et al.* Boron nitride substrates for high-quality graphene electronics. *Nat. Nanotechnol.* **5**, 722–726 (2010).
20. Das Sarma, S., Adam, S., Hwang, E. H. & Rossi, E. Electronic transport in two-dimensional graphene. *Rev. Mod. Phys.* **83**, 407–470 (2011).

21. Nilsson, J., Neto, A. H. C., Guinea, F. & Peres, N. M. R. Electronic Properties of Graphene Multilayers. *Phys. Rev. Lett.* **97**, 266801 (2006).
22. Miao, F. *et al.* Phase-Coherent Transport in Graphene Quantum Billiards. *Science* **317**, 1530–1533 (2007).
23. Tan, Y.-W. *et al.* Measurement of Scattering Rate and Minimum Conductivity in Graphene. *Phys. Rev. Lett.* **99**, 246803 (2007).
24. Martin, J. *et al.* Observation of electron-hole puddles in graphene using a scanning single-electron transistor. *Nat. Phys.* **4**, 144–148 (2008).
25. Chen, J.-H. *et al.* Charged-impurity scattering in graphene. *Nat. Phys.* **4**, 377–381 (2008).
26. Li, Q., Rossi, E. & Das Sarma, S. Two-dimensional electronic transport on the surface of three-dimensional topological insulators. *Phys. Rev. B* **86**, 235443 (2012).
27. Skinner, B., Chen, T. & Shklovskii, B. I. Effects of bulk charged impurities on the bulk and surface transport in three-dimensional topological insulators. *J. Exp. Theor. Phys.* **117**, 579–592 (2013).
28. Beidenkopf, H. *et al.* Spatial fluctuations of helical Dirac fermions on the surface of topological insulators. *Nat. Phys.* **7**, 939–943 (2011).
29. Gusev, G. M. *et al.* Nonlocal Transport Near Charge Neutrality Point in a Two-Dimensional Electron-Hole System. *Phys. Rev. Lett.* **108**, 226804 (2012).
30. Nichele, F. *et al.* Insulating State and Giant Nonlocal Response in an InAs/GaSb Quantum Well in the Quantum Hall Regime. *Phys. Rev. Lett.* **112**, 036802 (2014).
31. Chu, R.-L., Shi, J. & Shen, S.-Q. Surface edge state and half-quantized Hall conductance in topological insulators. *Phys. Rev. B* **84**, 085312 (2011).
32. Mendez, E. E., Esaki, L. & Chang, L. L. Quantum Hall Effect in a Two-Dimensional Electron-Hole Gas. *Phys. Rev. Lett.* **55**, 2216–2219 (1985).
33. Suzuki, K., Miyashita, S. & Hirayama, Y. Transport properties in asymmetric InAs/AlSb/GaSb electron-hole hybridized systems. *Phys. Rev. B* **67**, 195319 (2003).
34. Lee, D.-H. Surface States of Topological Insulators: The Dirac Fermion in Curved Two-Dimensional Spaces. *Phys. Rev. Lett.* **103**, 196804 (2009).
35. Vafek, O. Quantum Hall effect in a singly and doubly connected three-dimensional topological insulator. *Phys. Rev. B* **84**, 245417 (2011).
36. Zhang, Y.-Y., Wang, X.-R. & Xie, X. C. Three-dimensional topological insulator in a magnetic field: chiral side surface states and quantized Hall conductance. *J. Phys. Condens. Matter* **24**, 015004 (2012).
37. Brey, L. & Fertig, H. A. Electronic states of wires and slabs of topological insulators: Quantum Hall effects and edge transport. *Phys. Rev. B* **89**, 085305 (2014).
38. Morimoto, T., Furusaki, A. & Nagaosa, N. Charge and Spin Transport in Edge Channels of a $\nu = 0$ Quantum Hall System on the Surface of Topological Insulators. *Phys. Rev. Lett.* **114**, 146803 (2015).

39. Takashina, K. *et al.* Insulating states of a broken-gap two-dimensional electron-hole system. *Phys. Rev. B* **68**, 235303 (2003).
40. Anderson, P. W. Absence of Diffusion in Certain Random Lattices. *Phys. Rev.* **109**, 1492–1505 (1958).
41. Kurkijärvi, J. Hopping conductivity in one dimension. *Phys. Rev. B* **8**, 922–924 (1973).
42. Lee, P. A. Variable-range hopping in finite one-dimensional wires. *Phys. Rev. Lett.* **53**, 2042–2045 (1984).
43. Dunlap, D. H., Kundu, K. & Phillips, P. Absence of localization in certain statically disordered lattices in any spatial dimension. *Phys. Rev. B* **40**, 10999–11006 (1989).
44. Morimoto, T., Furusaki, A. & Nagaosa, N. Topological magnetoelectric effects in thin films of topological insulators. *Phys. Rev. B* **92**, 085113 (2015).
45. Wang, J., Lian, B., Qi, X.-L. & Zhang, S.-C. Quantized topological magnetoelectric effect of the zero-plateau quantum anomalous Hall state. *Phys. Rev. B* **92**, 081107 (2015).
46. Feng, Y. *et al.* Observation of the Zero Hall Plateau in a Quantum Anomalous Hall Insulator. *Phys. Rev. Lett.* **115**, 126801 (2015).
47. Kou, X. *et al.* Metal-to-insulator switching in quantum anomalous Hall states. *Nat. Commun.* **6**, 8474 (2015).
48. Baasanjav, D., Tretiakov, O. A. & Nomura, K. Magnetoelectric effect in topological insulator films beyond the linear response regime. *Phys. Rev. B* **90**, 045149 (2014).
49. Tilahun, D., Lee, B., Hankiewicz, E. M. & MacDonald, A. H. Quantum Hall Superfluids in Topological Insulator Thin Films. *Phys. Rev. Lett.* **107**, 246401 (2011).

Acknowledgements

We thank J. Hu, T. Wu, E. Palm, T. Murphy, A. Suslov, E. Choi and B. Pullum for experimental assistance. We also thank F. de Juan, R. Ilan, N. Nagaosa and W. Ku for helpful discussions. This work is supported by the DARPA MESO program (Grant N66001-11-1-4107). A portion of this work was performed at the National High Magnetic Field Laboratory, which is supported by National Science Foundation Cooperative Agreement No. DMR-1157490, the State of Florida, and the U.S. Department of Energy.

Author contributions

Y.P.C supervised the research. I.M. synthesized the crystals. Y.X. fabricated the devices, performed the transport measurements and analyzed the data. Y.X. and Y.P.C wrote the paper.

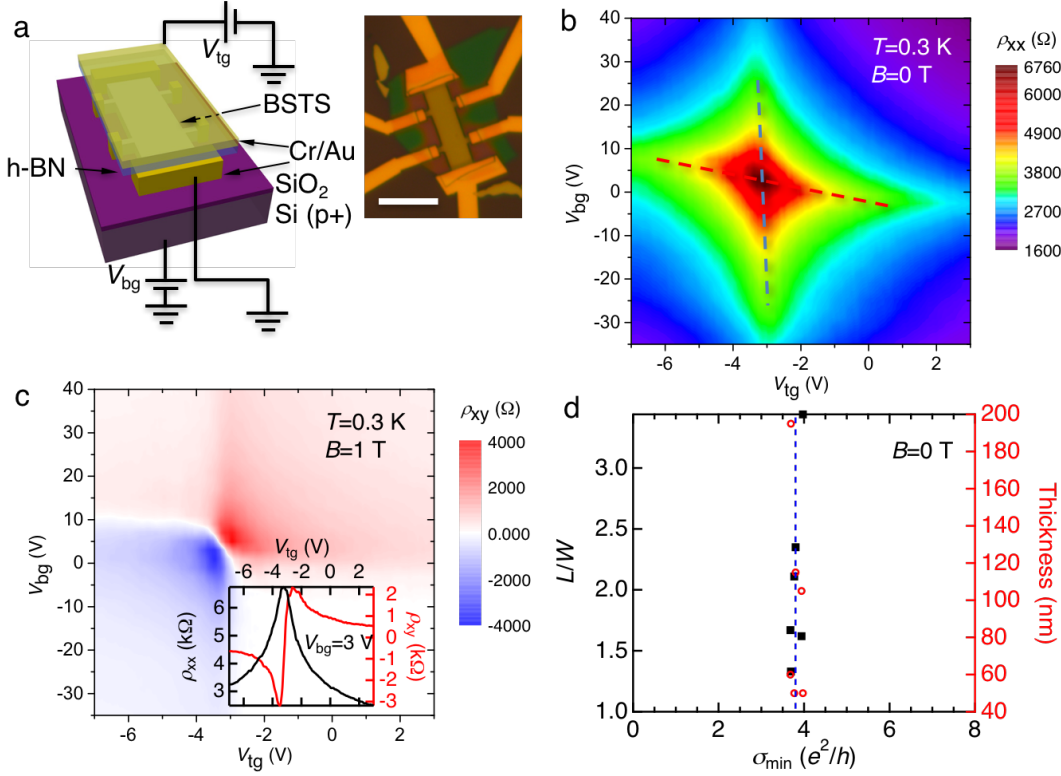


Figure 1 | Device configuration and dual-gated field effect at zero and low magnetic field. (a) Device schematic. Inset is an optical microscope image of a typical dual-gated BSTS device before depositing the top gate metal with scale bar 10 μm . (b, c) show 2D maps of ρ_{xx} at $B=0$ T and ρ_{xy} at $B=1$ T as functions of V_{tg} and V_{bg} on sample A. The blue (red) dashed lines in (b) are guides to the eye for the top (bottom) surface DP. The 2D map is generated by data measured from V_{tg} sweeps at a series of V_{bg} values, with one example at $V_{bg}=3$ V shown in the inset of (c). (d) Zero-magnetic-field minimum conductivity σ_{\min} (bottom axis) measured in 6 dual-gated samples at low temperature (<2 K) plotted as a function of the sample thickness (data in circles) and 2D aspect ratio (L/W , data in squares). The vertical dashed line indicates $3.8e^2/h$.

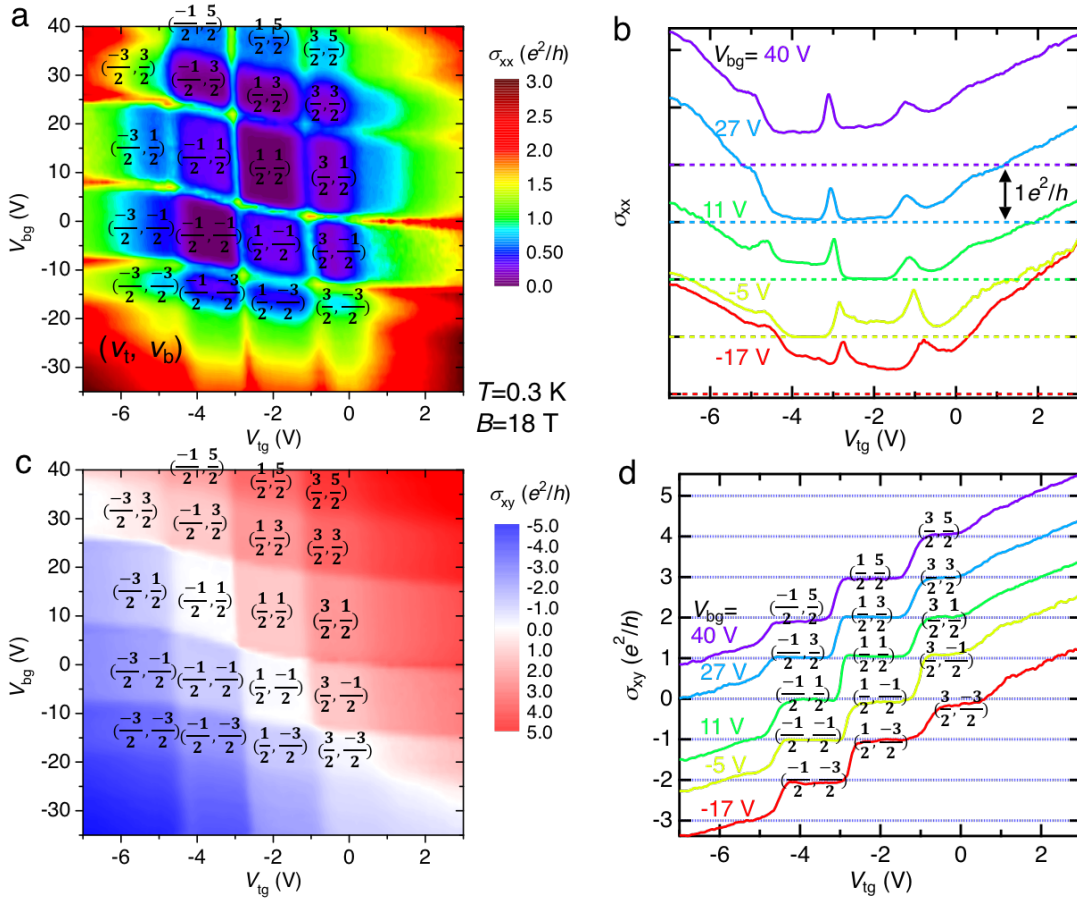


Figure 2 | Quantum Hall effect modulated by top and bottom gates. (a) σ_{xx} and (c) σ_{xy} , shown as 2D color maps, as functions of V_{tg} and V_{bg} at $B=18$ T and $T=0.3$ K in sample A, with representative cuts at 5 different values of V_{bg} shown in (b) and (d). The (ν_t, ν_b) labels (top, bottom) surface filling factors for corresponding quantum Hall states. The σ_{xx} curves in (b) are shifted vertically (in consecutive step of e^2/h) for clarity (the corresponding zero σ_{xx} levels are indicated by the same-colored horizontal dashed lines).

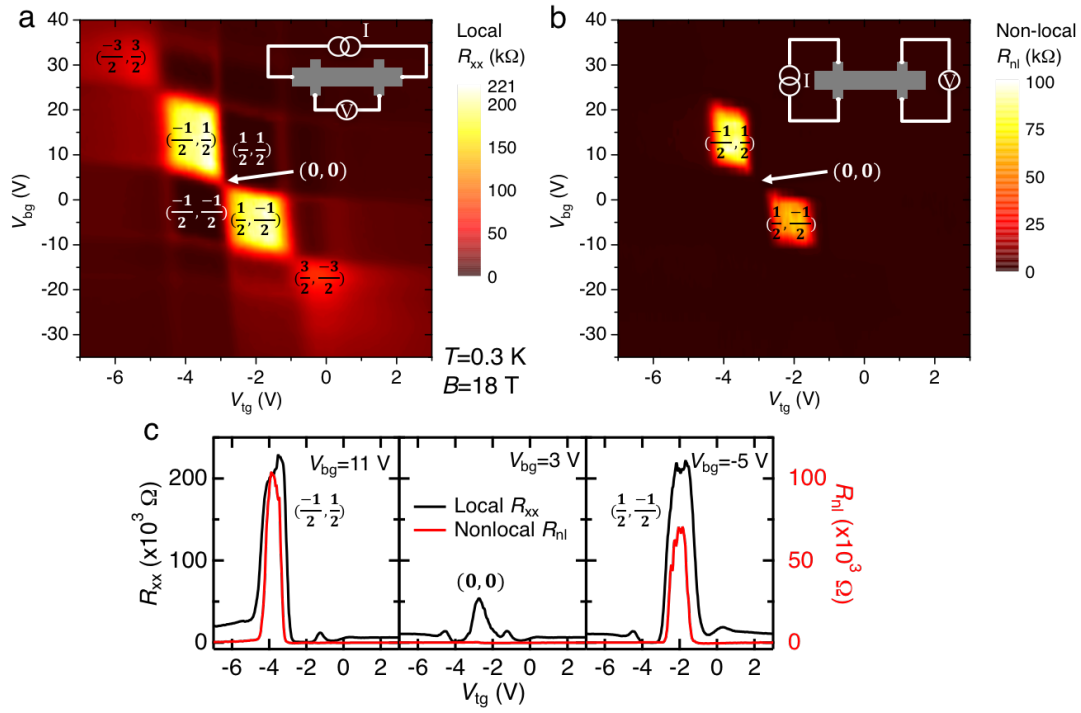


Figure 3 | Local and non-local resistance in dual-gated TI in high magnetic field. (a) Local resistance R_{xx} and **(b)** non-local resistance R_{nl} measured in sample A as functions of V_{tg} and V_{bg} at $B=18$ T and $T=0.3$ K, with insets showing the measurement setup schematics. **(c)** A few representative cuts of **(a)** and **(b)** at different values of V_{bg} . Filling factors for the local R_{xx} peaks are labeled in each sub-panel.

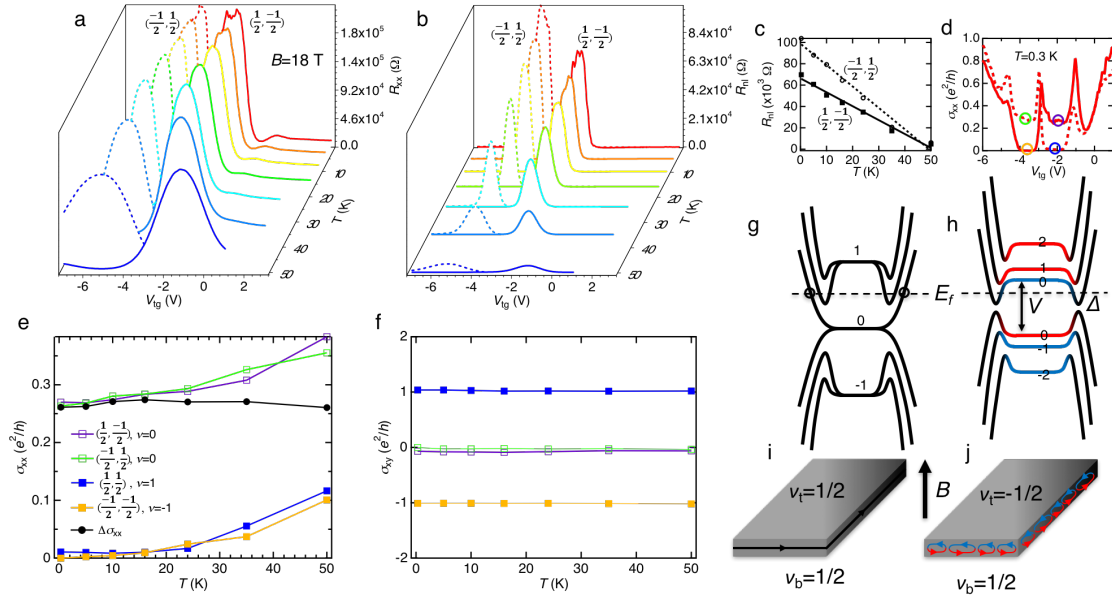
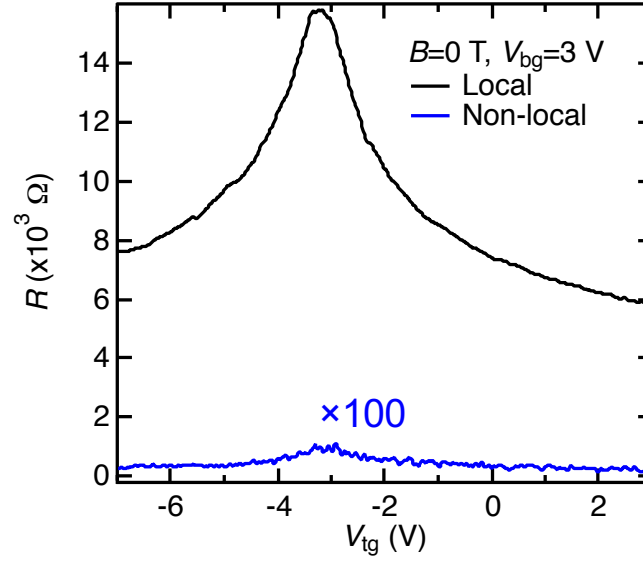
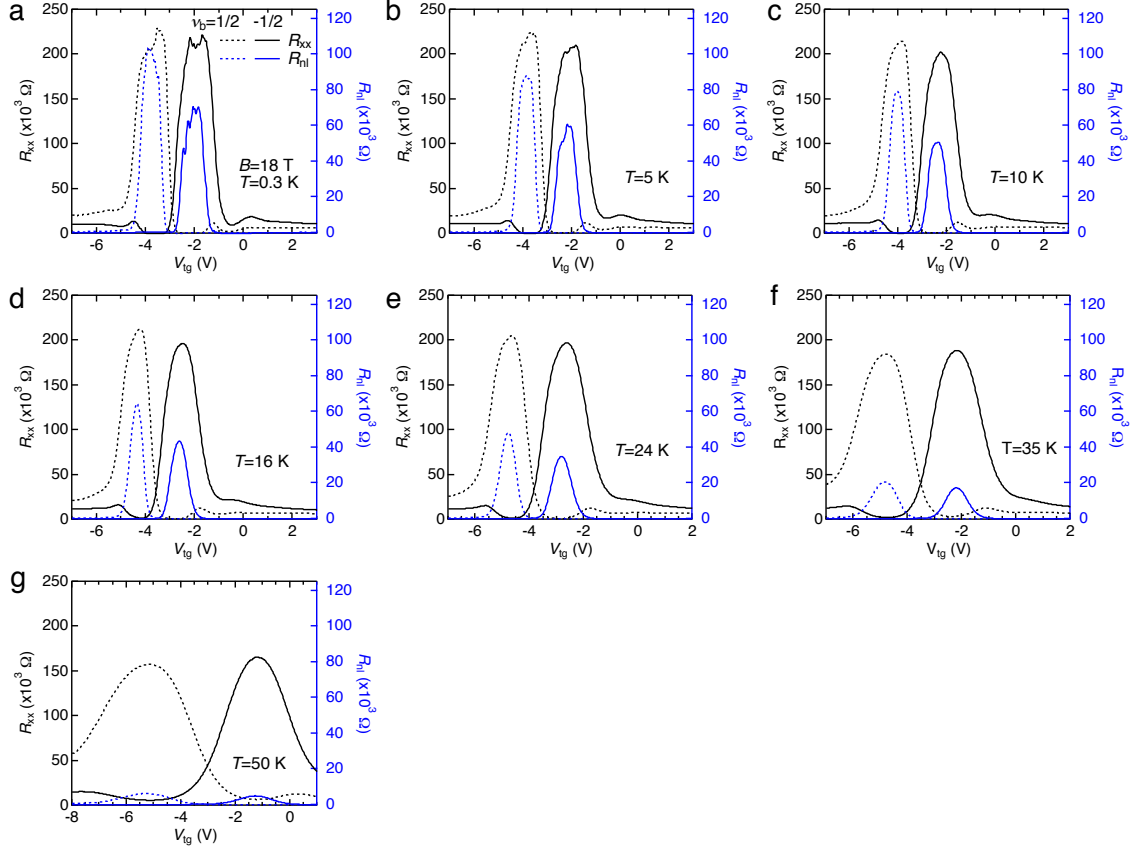


Figure 4 | Temperature dependence and illustrative schematics of the QHE and $\nu=0$ state in TI. (a) R_{xx} and (b) R_{nl} measured in sample A as functions of V_{tg} for different temperatures at $B=18$ T, where V_{bg} is chosen to set ν_b at $1/2$ (dashed lines) and $-1/2$ (solid lines), respectively. (c) The R_{nl} value at $(\nu_t, \nu_b)=(-1/2, 1/2)$ and $(1/2, -1/2)$ shows approximately linear dependence on temperature. (d) σ_{xx} versus V_{tg} (with the same two values of V_{bg} chosen in (a) and (b)) at $T=0.3$ K as an example, with each highlighted circle corresponding to a state in (e) plotted with corresponding colored symbols. (e) σ_{xx} and (f) σ_{xy} of $\nu=+1$, -1 and 0 states as functions of temperature. In (e), we also plot $\Delta\sigma_{xx}$ (difference between averaged $\nu=0$ states' σ_{xx} and averaged $\nu=\pm 1$ states' σ_{xx}), which barely changes with T . (g,h) Schematics of surface band structure (energy spectrum) in high magnetic field, showing Landau levels from top and bottom surfaces (blue and red) in the middle of the sample transitioning into side surface sub-bands at sample edge, and (i,j) edge states in a slab-shaped sample for $\nu=1$ and $\nu=0$ states. The dashed line indicates a representative Fermi level E_f and circles in (g) label chiral edge modes.

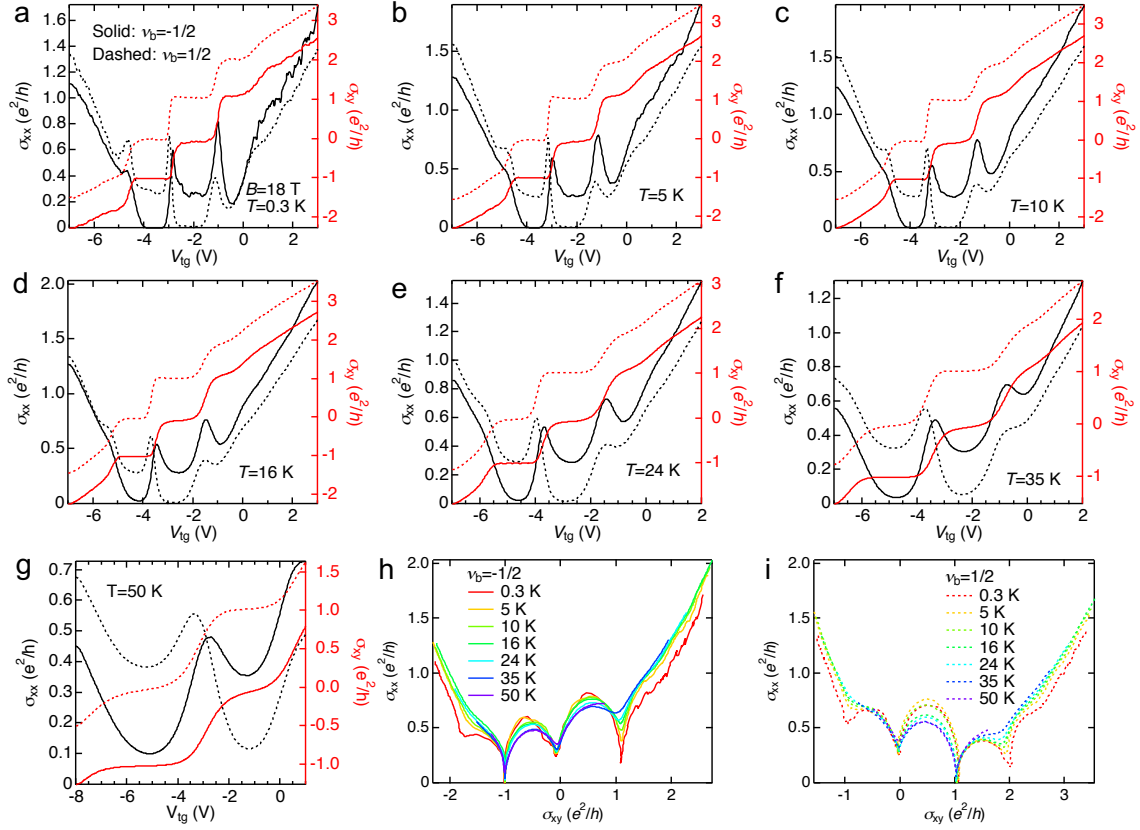
Supplementary Information



Supplementary Figure 1 | Measured local and nonlocal resistance without magnetic field. Local resistance R_{xx} (a) and non-local resistance R_{nl} (b) as functions of V_{tg} at $V_{bg}=3$ V and $B=0$ T, $T=0.3$ K. The non-local resistance R_{nl} shown here is multiplied by a factor of hundred. The data shown in this supplementary file are all from the same Sample A as that in the main text.



Supplementary Figure 2 | Temperature dependence of the local and nonlocal resistance. (a)-(g) Local resistance R_{xx} and nonlocal resistance R_{nl} versus V_{tg} at fixed bottom surface filling factor $\nu_b=1/2$ (dashed) and $-1/2$ (solid) measured at $B=18$ T at different temperatures. At total filling factor $\nu=0$ states, the nonlocal resistance R_{nl} decreases more rapidly with increasing temperature while the local resistance R_{xx} maintains large value up to 50 K.



Supplementary Figure 3 | Temperature dependence of the longitudinal and Hall resistivity. (a)-(g) Longitudinal conductivity σ_{xx} and Hall conductivity σ_{xy} versus V_{tg} at fixed bottom surface filling factor $\nu_b=1/2$ (dashed) and $-1/2$ (solid) measured at $B=18$ T at different temperatures. (h) and (i) show σ_{xx} versus σ_{xy} at $\nu_b=-1/2$ and $1/2$ respectively at different temperatures.